

LANDING AREA ANALYSIS FOR BALLISTIC LANDING TRAJECTORIES ON THE SECONDARY OF A BINARY ASTEROID

Iosto Fodde*, Jinglang Feng†, Massimiliano Vasile‡

Binary asteroid Didymos is the target of ESA's Hera mission, which plans to land a probe on the secondary body of the system, called Dimorphos. This procedure is planned to be performed using a ballistic landing strategy, which reduces the complexity of the spacecraft as no dedicated guidance, navigation, and control system is needed. However, these types of landings are sensitive to uncertainties in the deployment of the lander and the environment models. In this work, a robust ballistic landing trajectory design algorithm is developed, using a polynomial algebra based uncertainty propagation method. Furthermore, the results of this algorithm for different landing areas is compared to allow for the selection of the most robust landing location. The found minimum touchdown velocity and the dispersion of allowable deployment states are shown in different maps of the surface of Dimorphos. These maps show how the selected landing location affects the landing trajectories in different ways. Furthermore, the change in these maps for different magnitudes of the uncertainties in the gravitational parameter of the system and landing area are also obtained. It is shown that there are large areas on Dimorphos which allow low touchdown velocity landings, but which also have a relatively small dispersion of the deployment state. Other areas, mainly at higher latitudes, retain a low impact velocity landing while increasing the allowable deployment states. The region on Dimorphos facing the direction of motion around the primary gives the highest minimum touchdown velocity and are thus infeasible. The maps presented here allow for the selection of a landing location based on the uncertainties present in the system, and thus reduce the chance of failure of the landing.

INTRODUCTION

The combined NASA and ESA planetary defence mission, called the Asteroid Impact and Deflection Assessment (AIDA), plans to test a kinetic impactor deflection technique on the secondary of the binary asteroid system Didymos. The Didymos system consists of the primary body Didymos with a diameter of 780 meters, and the smaller moon called Dimorphos with a diameter of 160 meters. First, the NASA spacecraft DART will travel towards the system and impact with the secondary during a close approach with Earth to allow for Earth based observations of the change in orbital period due to the impact. Afterwards, ESA's Hera mission will rendezvous with the system and stay there for more in-depth observations of the system and the result of the impact. Two CubeSats will be deployed from the Hera spacecraft, which will perform a ballistic landing on Dimorphos at the end of the mission.¹

*PhD Researcher, Mechanical and Aerospace Engineering, University of Strathclyde, iosto.fodde@strath.ac.uk.

†Lecturer and Chancellor's Fellow, Mechanical and Aerospace Engineering, University of Strathclyde, jinglang.feng@strath.ac.uk.

‡Professor, Mechanical and Aerospace Engineering, University of Strathclyde, massimiliano.vasile@strath.ac.uk.

The main difficulties with the design of a landing system are the non-linear dynamics and the uncertainties in the physical properties of the system. Specifically, for a landing on the secondary body in a binary asteroid system, the procedure can be complicated due to the lower gravitational forces and the large influence of the primary body. The main advantage of a ballistic landing trajectory, i.e. with no active control of the translational state during descent, is that it requires no dedicated guidance, navigation, and control system. This is specifically beneficial in the case of a smaller CubeSat, as its size and mass budget are limited. The difficulty with ballistic landings is that small uncertainties in the deployment maneuver and in the parameters describing the dynamics of the system, e.g. the gravitational parameter of the bodies, can have a large effect on the final landing location.² Therefore, it is important to consider the effects of these uncertainties during the design of the landing trajectory.

This work develops a novel method to include the uncertainties in both the design of the ballistic landing trajectory itself and the selection of the landing site. Similar to the algorithm designed in,³ a minimum touchdown velocity for a certain location on the secondary is found using a bisection method. However, instead of a single point on the surface, a landing area is considered using the Generalised Intrusive Polynomial Algebra (GIPA) method. This method creates a polynomial expansion of the uncertain variables (e.g. landing location, primary and/or secondary mass), and propagates it through the dynamical system using an algebra over the space of polynomials. This method is more efficient compared to a Monte Carlo analysis, as only a single integration needs to be performed, instead of propagating a large number of samples. Furthermore, a surrogate model of the uncertain dynamics is created, which allows for a more in-depth analysis of the effect of the uncertainties on the trajectory.

Using GIPA, a minimum touchdown velocity is found for a landing area instead of a single landing point, taking into account the possible deviations in the environment from the nominal model as well. For each landing location, different parameters regarding the deployment maneuver can be analysed, e.g. the required accuracy of the ΔV direction and magnitude. This allows to generate a map that relates the desired landing location on the body with minimum touchdown velocities and deployment constraints. From this map, mission designers can select landing locations on the body which are less sensitive to uncertainties, and are thus more robust.

This paper is structured as follows: first the dynamics of the binary asteroid system Didymos is discussed. Afterwards, the robust trajectory design algorithm is explained in detail, specifically discussing the uncertainty propagation, bisection method, and deployment state analysis. Following, a set of maps of the surface of Dimorphos are discussed, considering different uncertainty setups. Finally, a conclusion based on these maps is given.

DYNAMICS

The Didymos (68503) binary system consists of the 780 meter diameter primary called Didymos and the 164 meter secondary Dimorphos. Some of the relevant physical properties of the binary system coming from recent observations can be found in Table 1. It is expected that the impact of DART will result in potentially significant changes to both the physical state of Dimorphos and its translational and rotational motion.⁴ As it is difficult to predict these changes beforehand, the current estimates will be used in the dynamical modelling of the system. The uncertainties considered in this work can be assumed to stem from both the current observations and the physical mis-modelling due to the DART impact.

Table 1: Relevant physical parameters of the Didymos system, taken from.⁵

System mass	$5.28 (\pm 0.54) \cdot 10^{11}$ kg
Mass ratio	0.0093 ± 0.0013
Didymos Diameter	$780 \text{ m} \pm 3 \text{ m}$
Didymos Rotational Period	$2.26 \text{ h} \pm 0.0001 \text{ h}$
Dimorphos Diameter	$164 \text{ m} \pm 18 \text{ m}$
Dimorphos Orbital Period	12 h
Body separation distance	1.19 km

As Dimorphos is observed to be in a nearly circular orbit around the primary, and the mass of the spacecraft is negligible compared to the two asteroids, the circular restricted three-body problem (CR3BP) is applied to model the system. In the CR3BP, a synodic reference frame that rotates together with the orbit of Dimorphos is considered. The origin of this frame is located in the barycentre of the system, the x -axis points towards Dimorphos, the z -axis to the orbit normal, and the y -axis completes the right-handed frame. The dynamics of the third body, given in the synodic frame, can be written as follows:⁶

$$\ddot{x} - 2\dot{y} = \frac{\partial U}{\partial x}, \quad (1)$$

$$\ddot{y} + 2\dot{x} = \frac{\partial U}{\partial y}, \quad (2)$$

$$\ddot{z} = \frac{\partial U}{\partial z}. \quad (3)$$

Here, the mass parameter $\mu = m_2/(m_1 + m_2)$, the body separation distance R , and the time constant $1/n$ (where n is the mean motion of Dimorphos) are used to obtain dimensionless parameters and simplify the equations to only include μ and the dimensionless coordinates x , y , and z . The potential U includes the rotational terms, and other forces acting on the third body. For the close proximity motion that is considered here, the gravitational forces from both asteroids dominate the dynamics compared to other forces like the Solar radiation pressure or the Solar gravity.⁷ Thus, only these forces are considered. The uncertainties in the gravitational forces considered in this work stem from both the estimation of the physical properties and the accuracy of the dynamical models. Therefore, a simple and more numerically efficient point mass gravity model is used, and the lower accuracy of this model compared to e.g. a polyhedron gravity model, is accounted for in the size of the uncertainties. The potential U in this case is given by:

$$U = \frac{1}{2}(x^2 + y^2) + \frac{1 - \mu}{r_1} + \frac{\mu}{r_2}, \quad (4)$$

where r_1 and r_2 represent the distance from the spacecraft to the primary and secondary, respectively.

The CR3BP allows an integral of motion called Jacobi's constant, given by:⁶

$$C = 2U - V^2, \quad (5)$$

where V is the velocity of the 3rd body. This variable can be seen as an energy measure, where lower values correspond to higher energy spacecraft trajectories. Constant values of $C = 2U$ give surfaces where the velocity of the spacecraft is zero and are called zero-velocity surface (ZVS). The ZVS restricts the motion of the spacecraft to certain regions in space, as is shown by the black lines in Figure 1. For high values of C , the ZVS blocks transport between the region around the two bodies, and between the inner regions and the region outside of the system (Figure 1a). As the energy of trajectories increases (decreasing value of C), the region near the first Lagrange point L_1 opens up to allow transport between the two bodies (Figure 1b). Increasing the energy even further opens the L_2 point, which then allows for the spacecraft to enter the inner region of the binary system (Figure 1c). Then, as C decreases more, the ZVS opens at the L_3 point (Figure 1d). For a given trajectory to be able to land on the surface of the secondary, C must have a sufficiently low value such that the ZVS is not blocking access to the surface through the L_2 point.⁸ Then the stable and unstable manifolds of the L_2 point can present feasible trajectories for landing.⁹

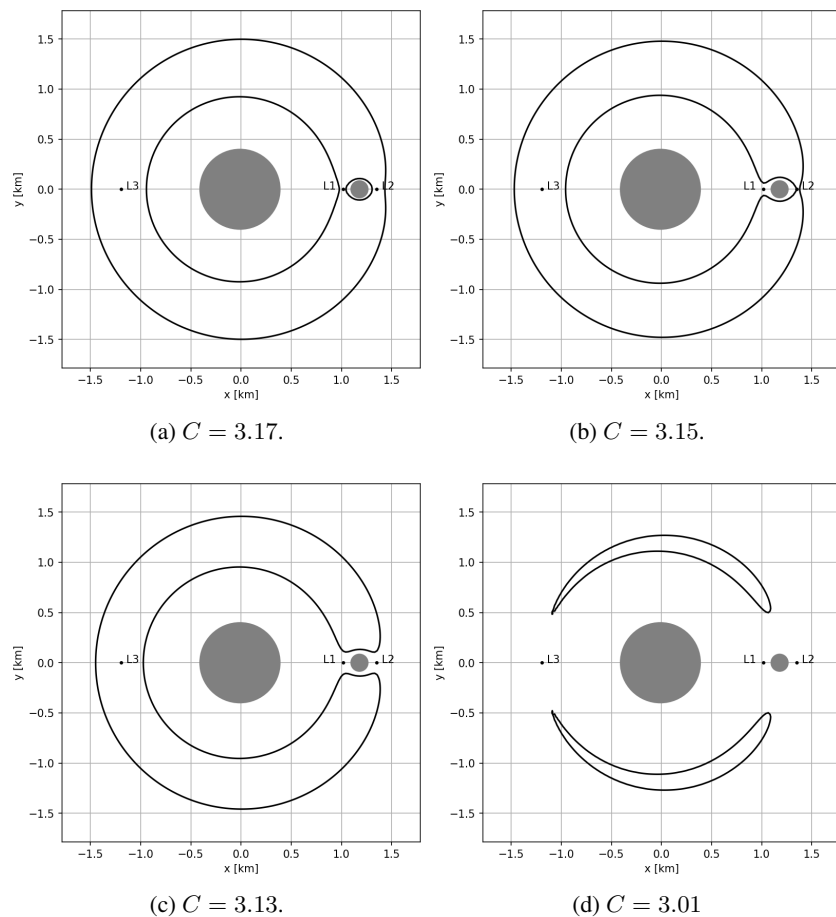


Figure 1: The ZVS plotted for four different Jacobi constant values.

LANDING TRAJECTORY DESIGN

The goal of the ballistic landing trajectory design process is to find a set of deployment conditions, i.e. the initial conditions of the lander, which guarantee the landing on the body under the considered

uncertainties, while minimizing the impact velocity at touchdown. For this purpose, an uncertainty propagation technique is needed to determine the effect of the uncertainties on the state over time. Then, this uncertainty propagation technique needs to be combined with a method to find a landing trajectory with minimum touchdown velocity. Finally, the resulting required deployment state needs to be analyzed in depth to determine the feasibility of performing this landing maneuver. This section discusses these individual steps and the resulting robust landing trajectory design algorithm.

Uncertainty Propagation

Consider a Cauchy problem defined as follows:

$$\begin{cases} \dot{\mathbf{x}} = \mathbf{f}(\mathbf{x}(t), \boldsymbol{\beta}, t) \\ \mathbf{x}(t_0) = \mathbf{x}_0 \end{cases} \quad (6)$$

where t is the time, \mathbf{x} is the state vector, and $\boldsymbol{\beta}$ is the dynamical model parameters. If the initial state \mathbf{x}_0 and model parameters $\boldsymbol{\beta}$ are uncertain, a set of N realisation or samples can be taken as follows: $[\mathbf{x}_{0,1}, \boldsymbol{\beta}_1, \dots, \mathbf{x}_{0,N}, \boldsymbol{\beta}_N]$. Propagating each sample through Eq.(6) until time t_f results in the trajectories $\mathbf{x}_i(t_f) = \phi_i(\mathbf{x}_{0,i}, \boldsymbol{\beta}_i, t_f)$.

The set of all possible trajectories at time t from the realisations of the uncertainty vector $\boldsymbol{\xi} = [\mathbf{x}_0, \boldsymbol{\beta}]$ within the uncertainty set $\Omega_{\boldsymbol{\xi}}$ can be defined as follows:

$$\Omega_t(\boldsymbol{\xi}) = \{\mathbf{x}(t) = \phi_i(\boldsymbol{\xi}, t) \mid \boldsymbol{\xi} \in \Omega_{\boldsymbol{\xi}}\}. \quad (7)$$

This set describes all the possible states at a certain time t as a result of the uncertainties. Therefore, to understand the effect of the uncertainties on this system, this set needs to be obtained.

The set of all possible initial states is given as follows:

$$\Omega_{\mathbf{x}_0} = \{\mathbf{x}(t_0, \boldsymbol{\xi}) \mid \boldsymbol{\xi} \in \Omega_{\boldsymbol{\xi}}\}. \quad (8)$$

Instead of propagating a number of individual trajectories from $\Omega_{\mathbf{x}_0}$ to analyse the effect of uncertainties on the ensemble of trajectories, the full set is propagated to obtain an analytical approximation of $\Omega_t(\boldsymbol{\xi})$. If \mathbf{x}_t is continuous in $\boldsymbol{\xi}$ and the set is compact, $\Omega_t(\boldsymbol{\xi})$ can be approximated using a polynomial function:

$$\tilde{\Omega}_t(\boldsymbol{\xi}) = P_{n,d}(\boldsymbol{\xi}) = \sum_{i=0}^{\mathcal{N}} c_i(t) \alpha_i(\boldsymbol{\xi}), \quad (9)$$

where $\alpha_i(\boldsymbol{\xi})$ are a set of multivariate polynomial basis functions, $c_i(t)$ are the corresponding coefficients, and $\mathcal{N} = \binom{n+d}{d}$ is the number of terms of the polynomial, where n is the degree of the polynomial and d is the number of variables. By taking a set of propagated samples, this polynomial can be obtained or constructed using methods like stochastic collocation or non-intrusive polynomial chaos methods. However, here the generalised intrusive polynomial algebra (GIPA) technique¹⁰ is used.

First, a specific polynomial basis α is selected and used to approximate the initial set $\Omega_{\mathbf{x}_0}$. To be able to propagate this set using the dynamics specified by $\mathbf{f}(\mathbf{x}(t), \boldsymbol{\beta}, t)$ in Eq. (6), the space

of polynomials $\mathcal{P}_{n,d}(\alpha)$ needs to be equipped with a set of elementary arithmetic operations. This enables the use of (numerical) integrators to propagate the polynomial function. Different options are available for the type of polynomials that can be used, e.g. Taylor polynomials,^{11,12} or Chebyshev polynomials,¹³ which require different implementations of the algebra. In GIPA, instead of defining a specific set of operations for each different polynomial basis, a change of basis is performed to a monomial basis ϕ . Its main advantage is that it significantly reduces the computational cost and makes sure that only one set of elementary arithmetic operations needs to be implemented.

A set of elementary functions, \otimes , corresponding to similar operations in a floating point algebra, $\oplus \in \{+, -, \cdot, /\}$, is combined with the function space $\mathcal{P}_{n,d}(\phi)$ to create an algebra. Then, given any two functions f_a and f_b , and their polynomial approximations F_a and F_b , the same operations between the two functions in the floating point algebra can be represented in the polynomial algebra:

$$f_a \oplus f_b \sim F_a \otimes F_b. \quad (10)$$

Besides the set of elementary operations, a set of elementary functions $h(y)$, e.g. $\{1/y, \sin(y), \exp(y), \log(y), \text{etc.}\}$, needs to be represented in the algebra as well. This can be done using the composition operator as follows:

$$h(\mathbf{f}(\mathbf{x})) \sim H(y) \circ F(\mathbf{x}), \quad (11)$$

where $H(y)$ is the univariate polynomial representation of $h(y)$ and $F(\mathbf{x})$ the polynomial algebra representation of the multivariate set $\mathbf{f}(\mathbf{x})$. The composition operator is defined as follows:

$$\circ : \mathcal{P}_{n,1}(\phi) \times \mathcal{P}_{n,d}(\phi) \rightarrow \mathcal{P}_{n,d}(\phi). \quad (12)$$

Compared to the elementary operations, the polynomial approximation of the elementary functions $H(y)$ differs between the chosen polynomial bases. In¹⁴ the accuracy of different polynomial bases for landing trajectories on Dimorphos were tested. From this analysis, the Chebyshev polynomial basis is selected for this work as it provides accurate results and is defined over a closed set. For a Chebyshev basis, an order 100 Chebyshev interpolation is used to obtain $H(y)$. For the Chebyshev interpolation an estimation of the range over which the expansion is taken is needed. This range estimation can either be done by taking the magnitude of the polynomial coefficients, or by taking a set of uniformly distributed random samples from the polynomial and saving the maximum and minimum values. It was shown in¹⁰ that the coefficient based method results in an overestimation of the range, which decreases the overall accuracy. The sampling based method does not suffer from this drawback, however it is less efficient compared to the coefficient based method. For this work, the sample based range method is selected as an accurate representation of the state is needed to obtain feasible landing trajectories.

The basic process of using GIPA for uncertainty propagation is now as follows. First a polynomial approximation is taken over the uncertain variables at the initial time using the Chebyshev basis. This basis is then transformed to the monomial basis to be able to use the general set of elementary operations, while using the elementary function approximation methods of Chebyshev polynomial basis. Using the desired numerical integrator, e.g. Runge-Kutta 4, the set can be propagated to the final desired time, using the algebra to replace each elementary operation and elementary function in the integrator and dynamical system. The convenience of this method is that no significant changes

need to be made to the implementation of the methods that are normally used to propagate a single trajectory, as only the elementary operations and functions need to be replaced, which can be done in several different coding languages by overloading the operations. Here, the SMART-UQ package is used for this,¹⁵ which contains implementations of the algebra for various different polynomial bases.

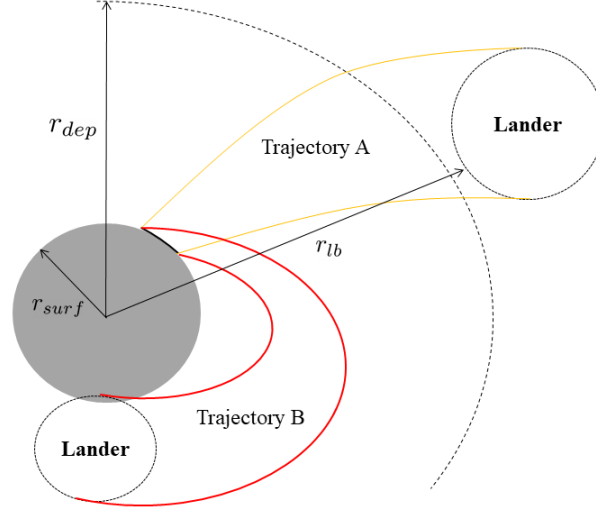


Figure 2: Diagram showing the robust ballistic landing trajectory design process.

Trajectory Design

Previously, a bisection algorithm was developed to find minimum touchdown velocity, v_l , trajectories.³ This method was further extended to include the effect of landing state and model uncertainties in.¹⁴ This method will also be applied in this work and is explained once more in this section for the sake of completeness.

Initially, the nominal touchdown latitude ϕ and longitude λ are selected. Together with these nominal landing conditions, the uncertainties to be included and their respective magnitudes are set. In this paper, uncertainties of the landing position ($\sigma_\phi, \sigma_\lambda$) and the gravitational parameters of both the primary Didymos and secondary Dimorphos ($\sigma_{\mu_p}, \sigma_{\mu_s}$) are considered. These uncertain parameters ξ are assumed to be bounded by σ_ξ . If ξ is distributed according to an infinite support function $\rho(\xi)$, the bounds can be taken so that $\int_{\Omega_\xi} \rho(\xi) d\xi < \varepsilon$, where ε is a given percentile.

To initialize the bisection algorithm, an initial guess for the upper and lower bound of the touchdown velocity is needed. The lower bound for the touchdown velocity, v_{lb} , is taken to be the minimum velocity needed to open up the ZVS around the L_2 point, for which an estimate is given by:³

$$v_{lb} = \sqrt{x^2 + y^2 + 2\frac{1-\mu}{r_1} + 2\frac{\mu}{r_2} - C_{L_2}}, \quad (13)$$

where C_{L_2} is the estimated value of the Jacobi constant at the L_2 point. The upper bound for the velocity v_{ub} is then taken to be a sufficiently large multiple of the lower bound.

For each iteration of the bisection algorithm, v_l is taken to be the middle point of v_{lb} and v_{ub} . Using the GIPA method, the uncertainties are then converted into a polynomial approximation and propagated backwards in time, i.e. from the time of landing back to the time of deployment, using the algebra. This is graphically shown in Figure 2. During the propagation, the distance between the surface of Dimorphos and the lower bound of the state uncertainty set, r_{lb} , is checked. If this lower bound is below the surface of Dimorphos (surface radius given by the sphere r_{surf}), the propagation is stopped and the current touchdown velocity becomes the lower bound for the next iteration of the bisection algorithm (see trajectory B in Figure 2). If the lower bound reaches a pre-defined safe deployment distance from Dimorphos, r_{dep} , the propagation stops and the current touchdown velocity becomes the touchdown velocity upper bound of the next iteration (see trajectory A in Figure 2). If after a maximum of 12 hours both of these events haven't happened, the propagation is stopped and the lower bound will be changed to the current touchdown velocity. This process is continued until the lower and upper bound of the touchdown velocity are sufficiently close (less than the value of TOL , which is taken as $1 \cdot 10^{-8}$). A summary of this process can be found in algorithm 1.

Algorithm 1 Robust trajectory design algorithm

```

Set  $v_{lb}, v_{ub}$ 
Set  $\phi \pm \sigma_\phi, \lambda \pm \sigma_\lambda$ 
Set  $\mu_p \pm \sigma_{\mu_p}, \mu_s \pm \sigma_{\mu_s}$ 
while  $|v_{ub} - v_{lb}| < TOL$  do
     $v_l = (v_{ub} + v_{lb})/2$ 
    Propagate  $\tilde{\Omega}_{x_f} \rightarrow \tilde{\Omega}_{x_0}$ 
    if  $r_{lb} < r_{surf}$  then
         $v_{lb} = v_l$ 
    else if  $r_{lb} > r_{dep}$  then
         $v_{ub} = v_l$ 
    else
         $v_{lb} = v_l$ 
    end if
end while

```

Deployment State

The landing trajectory design algorithm results in a set of states beyond the deployment distance corresponding to the minimal touchdown velocity trajectories considering the different uncertainties. The distribution of the allowed states at the time of deployment is an important quantity, as less stringent requirements on the spacecraft navigation and landing trajectory maneuver are needed if this set is large. This is shown graphically in Figure 3. Here, set A has a larger size at the deployment time compared to set B. Therefore, a wider spread of deployment states are possible for set A. Thus, the size of the set can give more information on the practicality of the obtained landing trajectory.

As the polynomial approximation of the deployment states can be transformed from monomial to Chebyshev basis, the orthogonality properties of this basis can be used to calculate the variance,

and therefore the size of the set. The Chebyshev polynomials $T_i(\xi)$ are orthogonal under the weight function $\rho(\xi) = (1 - \xi^2)^{-1/2}$ and are defined as follow:

$$\langle T_n, T_m \rangle = \int_{-1}^1 T_n(\xi) T_m(\xi) \rho(\xi) d\xi = \begin{cases} 1/2\pi\delta_{n,m} & \text{if } m \neq 0, n \neq 0 \\ \pi & \text{if } m = n = 0 \end{cases}, \quad (14)$$

where $\delta_{n,m}$ is the Kronecker delta function. Using the orthogonality properties, it can be found:

$$\bar{x}(t) = \mathbb{E}[x(t)] \approx \mathbb{E}[P_{n,d}(\boldsymbol{\xi})] = \int_{\Omega_{\boldsymbol{\xi}}} \left(\sum_{i=0}^{\mathcal{N}} c_i(t) T_i(\boldsymbol{\xi}) \right) \rho(\boldsymbol{\xi}) d\xi = c_0, \quad (15)$$

where the fact that $T_0 = 1$ and $\mathbb{E}[T_i] = 0, \forall i \neq 0$ is used. With this result, the second moment, or the variance, can be found in a similar matter:

$$\sigma^2 = \mathbb{E}[(x(t) - \bar{x}(t))^2] \quad (16)$$

$$\approx \int_{\Omega_{\boldsymbol{\xi}}} \left(\sum_{i=1}^{\mathcal{N}} c_i(t) T_i(\boldsymbol{\xi}) \right) \cdot \left(\sum_{i=1}^{\mathcal{N}} c_i(t) T_i(\boldsymbol{\xi}) \right) \rho(\boldsymbol{\xi}) d\xi \quad (17)$$

$$= \sum_{i=1}^{\mathcal{N}} \langle T_i, T_i \rangle c_i^2(t) = \sum_{i=1}^{\mathcal{N}} \frac{\pi}{2} c_i^2(t). \quad (18)$$

Where $\langle T_i, T_i \rangle = \frac{\pi}{2}$ comes from Eq. (14) and the fact that only degrees of $i > 0$ are used due to the subtraction of the mean. In the case of a multivariate system, the coefficients c_i become vectors and the outer product is taken to obtain the covariance matrix:

$$\Sigma = \sum_{i=1}^{\mathcal{N}} \frac{\pi}{2} \mathbf{c}_i \mathbf{c}_i^T. \quad (19)$$

The eigenvalues of Σ give information on the relative size of the state set at the deployment time. A measure of this covariance based size is defined here as follows:

$$\bar{\eta} = \sum_i \eta_i, \quad (20)$$

where η_i are the eigenvalues of Σ . Now, $\bar{\eta}$ can be used to compare the spread of the deployment state for different landing trajectories.

RESULTS

Using the trajectory design algorithm discussed previously, different landing locations and uncertainties are analysed. A set of maps which link the targeted landing location with a certain performance parameter are discussed. Furthermore, the effect of different uncertain parameters and their magnitudes on these maps are analysed as well.

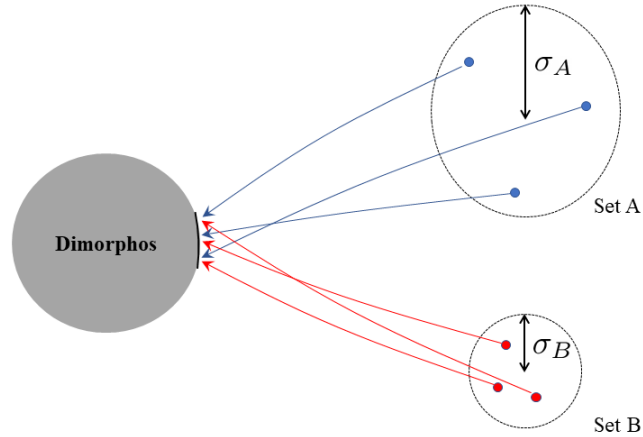


Figure 3: Diagram showing two deployment sets, A and B, with different sizes represented by the variances σ_A and σ_B respectively. A couple of realisations of these trajectories are shown as well, blue for trajectories of set A and red for the ones of set B. In this case, $\sigma_A > \sigma_B$ thus there is a wider range of possible deployment states that result in a landing for A compared to that of B.

Touchdown Velocity

The minimum touchdown velocity parameter shows the required impact velocity to ensure that all initial landing states are able to land in the desired landing area from the deployment distance. A high value for the touchdown velocity does not necessarily mean that there aren't different individual trajectories that are able to land in this region with a lower velocity. However, the touchdown velocities given here guarantee that all the trajectories will land in the given region with the found touchdown velocity considering the uncertainties.

For a better comparison, the map for the touchdown velocities considering no uncertainties is given in Figure 4a. The three other cases considered are 5 degree uncertainty in both the landing latitude and longitude (see Figure 4c), 10 percent uncertainty in the gravitational parameters μ of both bodies (see Figure 4d), and the combination of both uncertainties (see Figure 4b). The large white regions in all maps represent regions where no feasible landing trajectories were found. It can be seen that for all cases there are large regions of low touchdown velocities around 0 degree longitude and latitude. The touchdown velocity in this region is also similar to the ones found in Figure 4a, showing that the found robust landing trajectories do not have a more significant impact, even though all the different uncertainties are considered. From around 50 degrees to 100 degrees longitude there is a region of high impact velocity. This region is on the side of Dimorphos facing the direction of its motion. Therefore, a higher relative velocity is expected. For this region, the differences among different cases is larger. A map of the differences in touchdown velocity is shown in Figure 5. For higher latitudes in the high touchdown velocity case there are small regions (deep red) where there are significantly higher velocity impacts in the case of gravitational uncertainty.

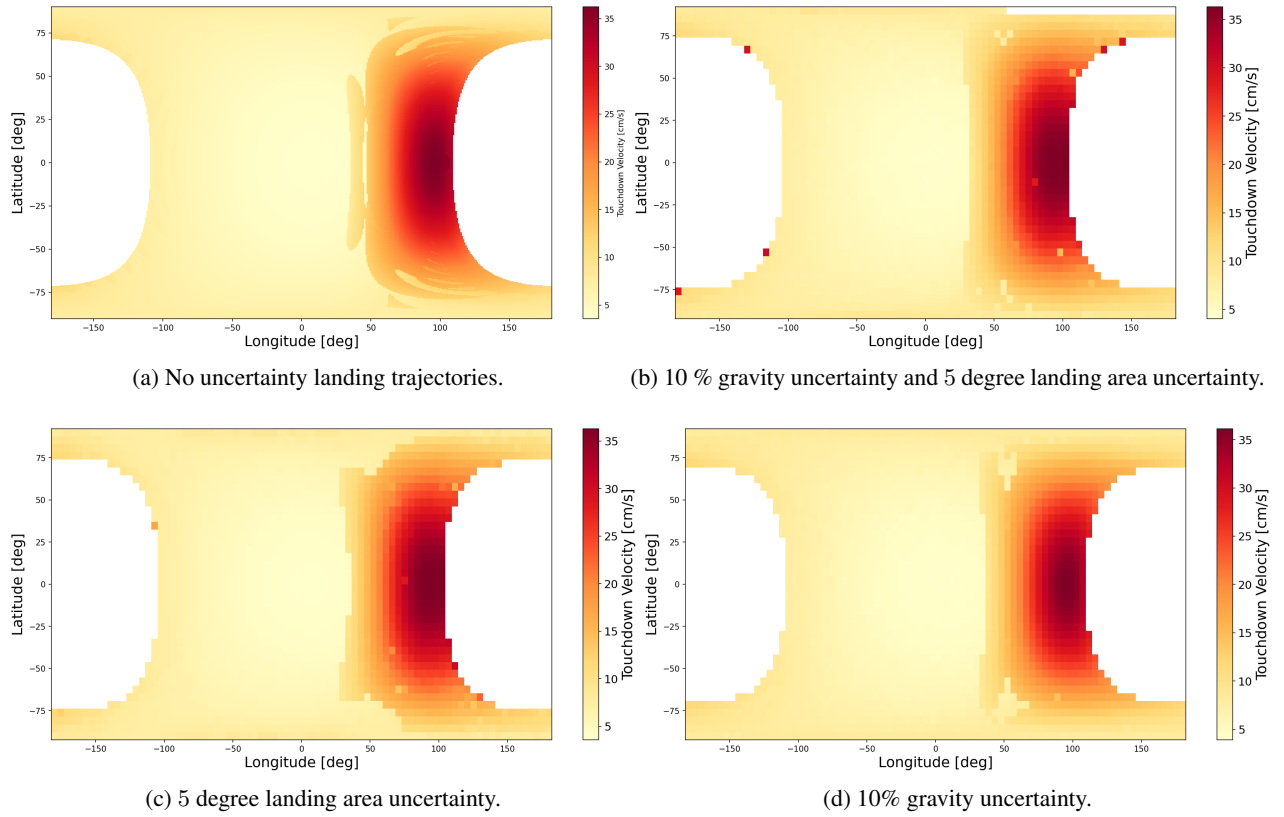


Figure 4: Minimum touchdown velocity maps considering different or no uncertainties.

For the lower latitudes in this region, the 5 degree landing area uncertainty has higher touchdown velocities as can be seen by the negative values.

In Figure 6, two examples are given from the two different regions discussed previously. Figure 6a shows a set of 50 sample trajectories taken from the final landing trajectory polynomial for the 0 degree latitude and longitude location. There are a couple of trajectories which perform an orbit around the L_2 point before leaving the area around the secondary and reaching the deployment distance. In contrast, other trajectories in this set follow a more direct path out of the system. The trajectories for the landing area facing the direction of motion are shown in Figure 6b. In this case, a large part of an orbit around the system needs to be performed to reach the landing area. The opposite direction of the velocity between the lander and the secondary increases the impact velocity for this landing area.

The effect of larger landing areas can be seen in Figure 7a for a 10 degree uncertainty, and in Figure 7b for a 20 degree uncertainty. For these cases there is an overall increase in touchdown velocity for most of the landing areas. Specifically for the 20 degree uncertainty case, the poles of Dimorphos see a significant increase in the minimum allowable touchdown velocity. The low latitude cases are less affected and still show large regions of low impact velocity.

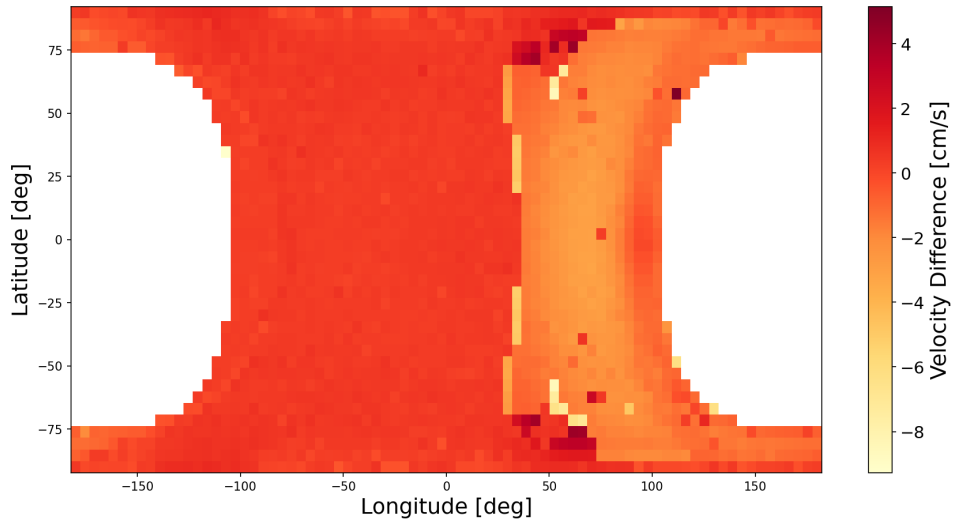
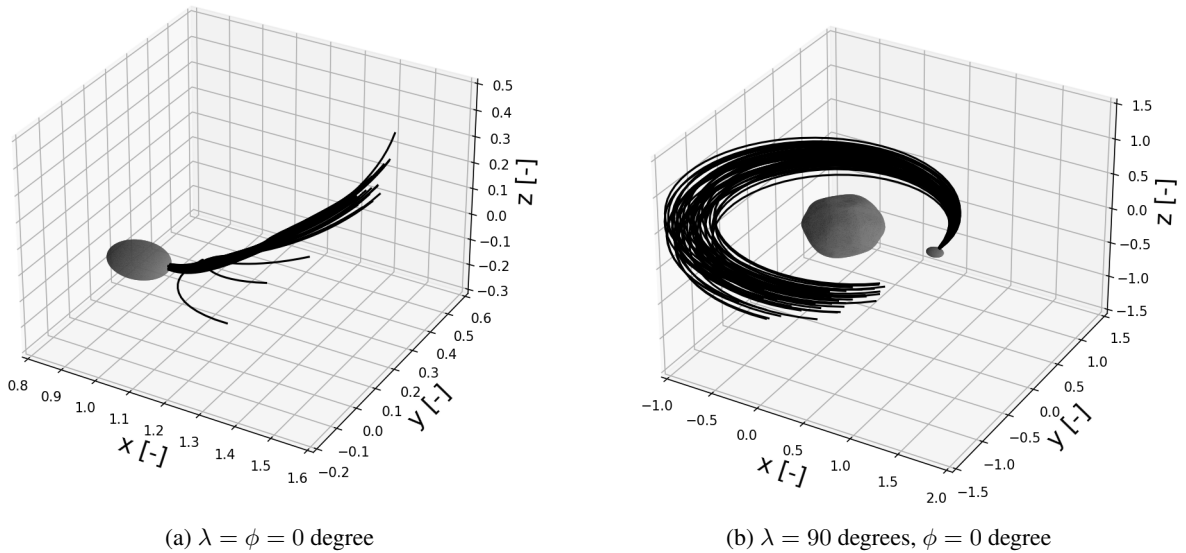


Figure 5: Difference in touchdown velocity between 10% gravity uncertainty and 5 degree landing uncertainty. Positive values indicate higher touchdown velocities for the 10% gravity uncertainty case and vice versa.



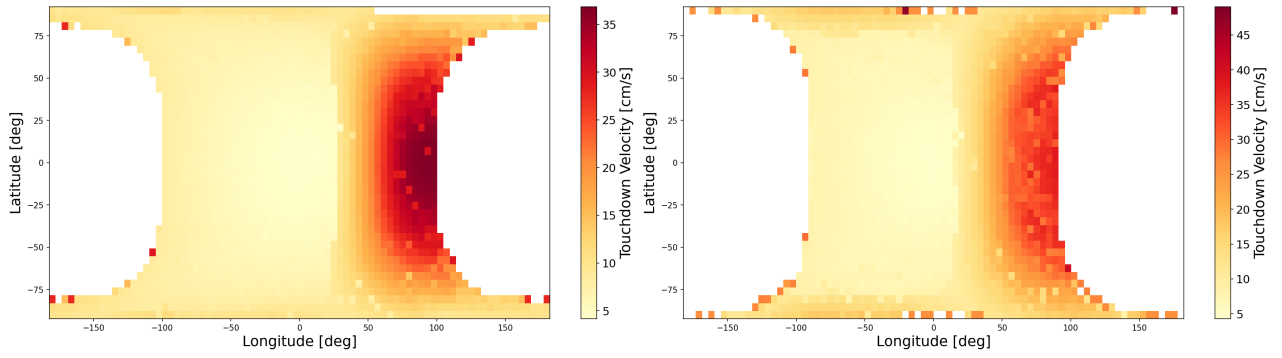
(a) $\lambda = \phi = 0$ degree

(b) $\lambda = 90$ degrees, $\phi = 0$ degree

Figure 6: Example trajectories from different regions of the 5 degree landing area and 10% gravity uncertainty maps.

Deployment State Dispersion

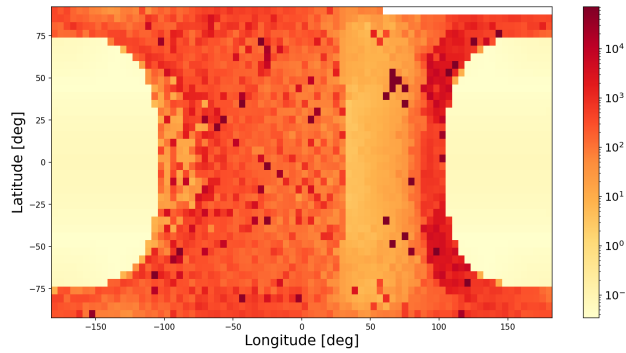
The deployment state dispersion, indicated by $\bar{\eta}$ defined in Eq. (20), shows how much the trajectories have moved apart from each other going from the landing area towards the deployment region, i.e. backwards in time. A large value of $\bar{\eta}$ for a specific landing area thus shows that there are a large amount of allowable deployment states which result in the minimum touchdown velocity found in the previous section.



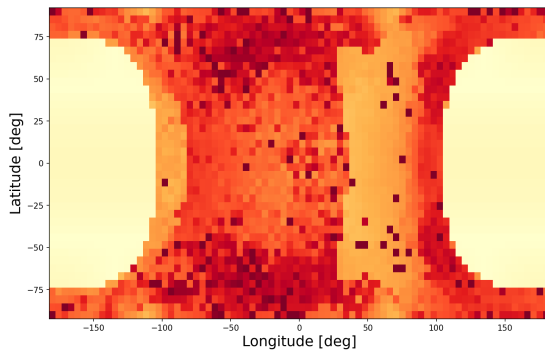
(a) 10 degree landing area uncertainty.

(b) 20 degree landing area uncertainty.

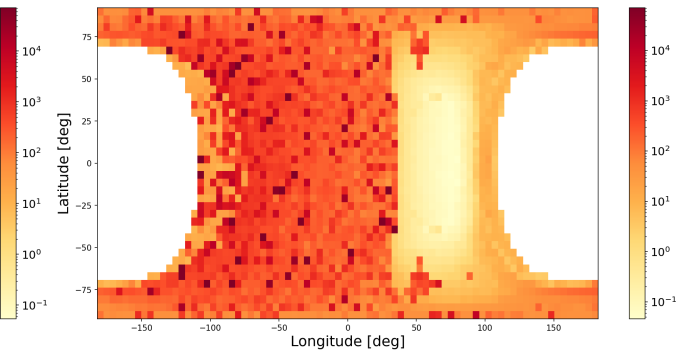
Figure 7: The maps for increasing landing area size, considering 10% uncertainty in the gravity as well.



(a) 10 % gravity uncertainty and 5 degree landing area uncertainty.



(b) 5 degree landing area uncertainty.



(c) 10% gravity uncertainty.

Figure 8: $\bar{\eta}$ maps considering different uncertainties.

Figure 8 shows $\bar{\eta}$ for the first three cases. Due to the high velocity, and therefore faster time of flight, the regions of high touchdown velocity correspond to low values of the deployment state dispersion. The low touchdown velocity, however, sees much higher deployment state dispersion. This can be verified as well in the example trajectories of Figure 6, where the 0 degree latitude and longitude case has different trajectories within the set that have significantly different behaviour as a

small subset of trajectories orbit the L_2 point before escaping. Even though the trajectories in the 90 degree longitude case do disperse, they have relatively similar behaviour and thus they stay relatively close together. Another effect that can be observed is the high values of $\bar{\eta}$ in the case of Figure 8b for the higher latitudes. Similar effects are observed for the higher landing area uncertainty cases in Figure 9. To understand the reason for the high $\bar{\eta}$ in high latitude landing areas, two example trajectories from the 20 degree landing area uncertainty of Figure 9 are taken and shown in Figure 10. The first set of sample landing trajectories, Figure 10a, are taken for the 0 degree latitude case with the landing area on the side opposite the direction of motion of Dimorphos. These trajectories have a relatively similar behaviour, and thus remain closer together. The high latitude case for the same longitude, Figure 10b, has a part of the trajectories first move in the z direction and others that immediately move in other directions. This shows that the trajectories that target this landing site can land from a large number of different directions.

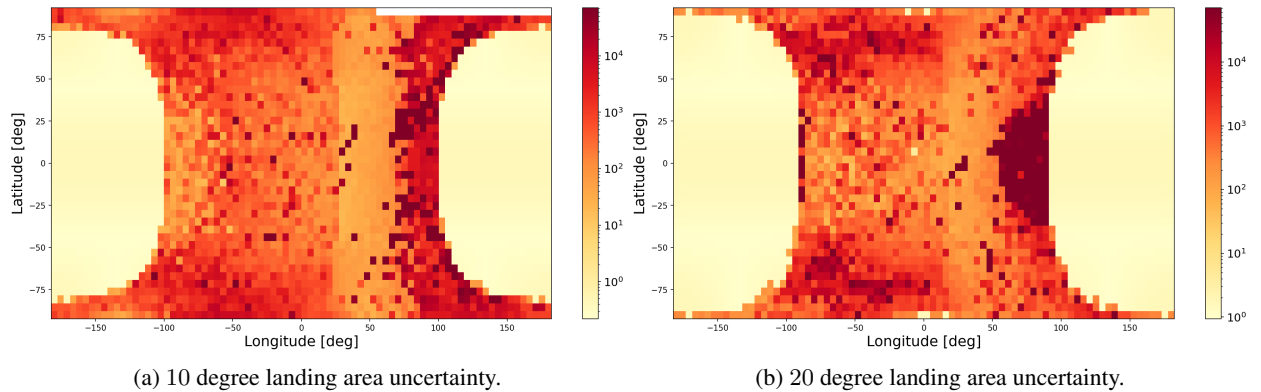


Figure 9: The $\bar{\eta}$ maps for increasing landing area size, considering 10% uncertainty in the gravity as well.

CONCLUSION

This paper studies the problem of designing ballistic landing trajectories for landing on the asteroid Dimorphos considering significant uncertainties in both the model parameters and state of the lander. A robust landing trajectory design method was developed to find minimum touchdown velocity trajectories for different landing locations and uncertainties. It was shown how maps of the surface of Dimorphos can be made that show the properties of the landing trajectories for the different landing locations.

It was found that there are large areas of the surface of Dimorphos where low impact velocities of around 5 cm/s are found, even considering large uncertainties in the strength of the gravity field and landing location. Near the side facing the direction of motion of Dimorphos, the touchdown velocities start to increase significantly. This region starts to grow larger in the higher latitudes as the uncertainties start to become more significant. Additionally, increasing the allowable landing area increases the touchdown velocities for a large amount of areas, especially around the poles of Dimorphos.

The dispersion of deployment states was investigated as well. Low touchdown velocity areas were found to correspond to larger distributions and vice versa for high touchdown velocities. For larger

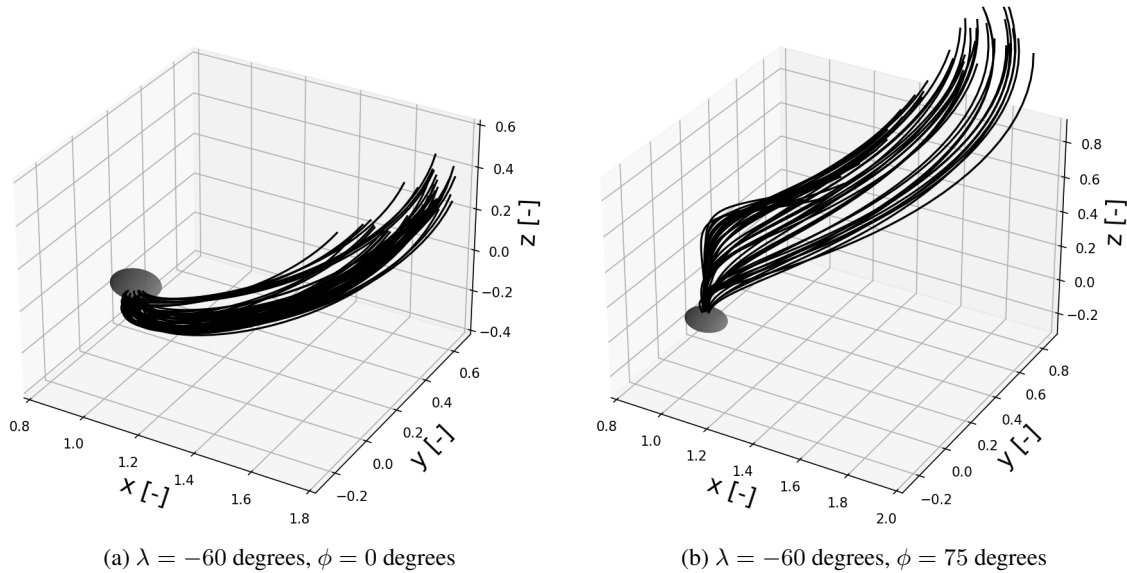


Figure 10: Example trajectories from different regions of the 20 degree landing area and 10 degree gravity uncertainty maps.

landing areas, regions in the higher latitudes of Dimorphos were found which show significantly larger deployment state dispersion as these trajectories come in from various different directions.

In conclusion, this paper demonstrates a new method of developing robust ballistic landing trajectories and analyses their sensitivities to different landing locations and uncertainties. This method can be used in future studies about landing on small bodies and allows mission designers to consider the risk due to uncertainties during the selection of a landing site.

ACKNOWLEDGMENT

The authors would like to acknowledge the ESA OSIP program for partly sponsoring this research project. Furthermore, the authors are grateful to Jesus Gil-Fernandez for his help and advice on Hera, Juventas, and the landing procedure as a whole.

REFERENCES

- [1] H. Goldberg, o. Karatekin, B. Ritter, A. Herique, P. Tortora, C. Prioroc, B. Gutierrez, P. Martino, and I. Carnelli, "The Juventas CubeSat in Support of ESA's Hera Mission to the Asteroid Didymos," *Small Satellite Conference*, 8 2019.
- [2] O. Çelik, O. Karatekin, B. Ritter, and J.-P. Sánchez, "Reliability Analysis of Ballistic Landing in Binary Asteroid 65803 (1996GT) Didymos under Uncertainty and GNC Error Considerations," 2017.
- [3] O. Çelik and J. P. Sánchez, "Opportunities for ballistic soft landing in binary asteroids," *Journal of Guidance, Control, and Dynamics*, Vol. 40, 4 2017, pp. 1390–1402, 10.2514/1.G002181.
- [4] H. F. Agrusa, I. Gkolias, K. Tsiganis, D. C. Richardson, A. J. Meyer, D. J. Scheeres, M. Čuk, S. A. Jacobson, P. Michel, O. Karatekin, A. F. Cheng, M. Hirabayashi, Y. Zhang, E. G. Fahnestock, and A. B. Davis, "The excited spin state of Dimorphos resulting from the DART impact," *Icarus*, Vol. 370, 12 2021, p. 114624, 10.1016/J.ICARUS.2021.114624.
- [5] "Hera Didymos Reference Model Issue 5," tech. rep., ESA, 2020.
- [6] K. Wakker, *Fundamentals of Astrodynamics*. Delft: Institutional Repository Delft University of Technology, 1 2015.

- [7] F. Ferrari, V. Franzese, M. Pugliatti, C. Giordano, and F. Topputo, “Trajectory Options for Hera’s Milani CubeSat Around (65803) Didymos,” *The Journal of the Astronautical Sciences*, 9 2021, pp. 1–22, 10.1007/S40295-021-00282-Z.
- [8] S. Tardivel and D. J. Scheeres, “Ballistic deployment of science packages on binary asteroids,” *Journal of Guidance, Control, and Dynamics*, Vol. 36, 4 2013, pp. 700–709, 10.2514/1.59106/ASSET/IMAGES/LARGE/FIGURE10.JPEG.
- [9] D. Villegas Pinto, D. Hestroffer, E. Canalias, and F. Capolupo, “Deployment of small-body landers from terminator orbits in perturbed environments,” *AAS/AIAA Astrodynamics Specialist Conference*, Virtual Lake Tahoe, 4 2020.
- [10] M. Vasile, C. O. Absil, and A. Riccardi, “Set propagation in dynamical systems with generalised polynomial algebra and its computational complexity,” *Communications in Nonlinear Science and Numerical Simulation*, Vol. 75, 8 2019, pp. 22–49, 10.1016/j.cnsns.2019.03.019.
- [11] M. Valli, R. Armellin, P. Di Lizia, and M. R. Lavagna, “Nonlinear mapping of uncertainties in celestial mechanics,” *Journal of Guidance, Control, and Dynamics*, Vol. 36, 1 2013, pp. 48–63, 10.2514/1.58068.
- [12] D. Pérez-Palau, J. J. Masdemont, and G. Gómez, “Tools to detect structures in dynamical systems using Jet Transport,” *Celestial Mechanics and Dynamical Astronomy*, Vol. 123, 11 2015, pp. 239–262, 10.1007/s10569-015-9634-3.
- [13] A. Riccardi, C. Tardioli, and M. Vasile, “An intrusive approach to uncertainty propagation in orbital mechanics based on tchebycheff polynomial algebra,” *Advances in the Astronautical Sciences*, Vol. 156, Vail, Univelt Inc., 2016, pp. 707–722.
- [14] I. Fodde, J. Feng, and M. Vasile, “Robust Trajectory Design for Ballistic Landings on Dimorphos.,” *AIAA Science and Technology Forum and Exposition, AIAA SciTech Forum 2022*, 2022, 10.2514/6.2022-1476.
- [15] C. O. Absil, A. Riccardi, M. Vasile, and C. Tardioli, “SMART-UQ: uncertainty quantification toolbox for generalised intrusive and non intrusive polynomial algebra,” *6th International Conference on Astrodynamics Tools and Techniques*, Darmstadt, Germany, 3 2016.